Journal of Membrane Science 588 (2019) 117200

Contents lists available at ScienceDirect

Journal of Membrane Science

journal homepage: www.elsevier.com/locate/memsci

Facile Cu-BTC surface modification of thin chitosan film coated polyethersulfone membranes with improved antifouling properties for sustainable removal of manganese

Mohammad Mozafari[a,1], S. Fatemeh Seyedpour[a,1], Saeed Khoshhal Salestan[a], Ahmad Rahimpour[a,b,c,*], Ahmad Arabi Shamsabadi[d], Mostafa Dadashi Firouzjaei[e], Milad Rabbani Esfahani[e], Alberto Tiraferri[c,**], Hamed Mohsenian[a], Marco Sangermano[b], Masoud Soroush[d,***]

[a] *Department of Chemical Engineering, Babol Noshirvani University of Technology, Shariati Ave., Babol, 4714871167, Iran*
[b] *Department of Applied Science and Technology, Politecnico di Torino, Corso Duca Degli Abruzzi 24, 10129, Turin, Italy*
[c] *Department of Environment, Land and Infrastructure Engineering (DIATI), Politecnico di Torino, Corso Duca Degli Abruzzi 24, 10129, Turin, Italy*
[d] *Department of Chemical and Biological Engineering, Drexel University, Philadelphia, PA, 19104, USA*
[e] *Department of Chemical and Biological Engineering, The University of Alabama, Tuscaloosa, AL, 35487, USA*

ARTICLE INFO

Keywords:
Cu-BTC clusters
Chitosan
Membrane functionalization
Manganese removal
Antifouling properties

ABSTRACT

Loose nanofiltration membranes, which have a loose selective layer and desired surface charge, provide high water flux and significant retention of low molecular weight molecules. In this study, a thin film of copper (II)-benzene-1,3,5-tricarboxylate (Cu-BTC) clusters was anchored on the surface of a chitosan (CS)-coated polyethersulfone (PES) membrane to improve the surface properties as well as performance (permeability, heavy metal removal efficiency, and antifouling activity) of the membrane. Characterization techniques, such as FE-SEM, EDX, XPS and AFM, zeta potential and water contact-angle measurements, verified that Cu-BTC was successfully anchored on the CS layer. The Cu-BTC/CS membrane exhibited higher surface hydrophilicity and roughness compared to the pristine one. It also demonstrated a water flux of $44\,\mathrm{L\,m^{-2}h^{-1}}$ and a manganese removal efficiency of 86%, while the membrane coated only with CS had an average water flux of $39\,\mathrm{L\,m^{-2}h^{-1}}$ and a manganese removal efficiency of 78%. Compatibility and interfacial interactions between the Cu-BTC clusters and the CS layer were investigated using molecular dynamics (MD). MD simulations indicated that the Cu-BTC clusters increased the affinity of the membrane for water molecules. The anchored Cu-BTC clusters also improved the antibacterial activity of the membrane; the Cu-BTC/CS membrane inactivated 83% of *Escherichia coli* bacteria, while the pristine CS membrane 47% of the bacteria. The Cu-BTC/CS membrane also demonstrated interesting anti-fouling properties against both organic and biological foulants.

1. Introduction

Loose nanofiltration (NF) membranes, which have a loose selective layer and controlled surface charge, provide high water flux and significant retention of low molecular weight molecules [1,2]. They are used, for example, in dye/salt removal [3]. Surface modification of membranes is an effective technique to tailor the surface properties and enhance permeability, selectivity, and the antifouling activity of the membranes. A practical approach to modifying the structure of a membrane to improve the membrane performance is to embed a flexible polymer with nanomaterials [4]. However, poor compatibility between the matrix of polymeric membranes and inorganic nanomaterials partially impair the retention performance and limit the potential antifouling activity of the modifying materials [5].

---

[*] Corresponding author. Department of Chemical Engineering, Babol Noshirvani University of Technology, Shariati Ave., Babol, 4714871167, Iran.

[**] Corresponding author. Department of Environment, Land and Infrastructure Engineering (DIATI), Politecnico di Torino, Corso Duca Degli Abruzzi 24, 10129, Turin, Italy.

[***] Corresponding author. Department of Chemical and Biological Engineering, Drexel University, Philadelphia, PA, 19104, USA.

E-mail addresses: ahmadrahimpour@nit.ac.ir, ahmad.rahimpour@polito.it (A. Rahimpour), alberto.tiraferri@polito.it (A. Tiraferri), soroushm@drexel.edu (M. Soroush).

[1] M.M. and S.F.S. contributed equally to this work.

https://doi.org/10.1016/j.memsci.2019.117200
Received 1 May 2019; Received in revised form 18 June 2019; Accepted 18 June 2019
Available online 19 June 2019
0376-7388/

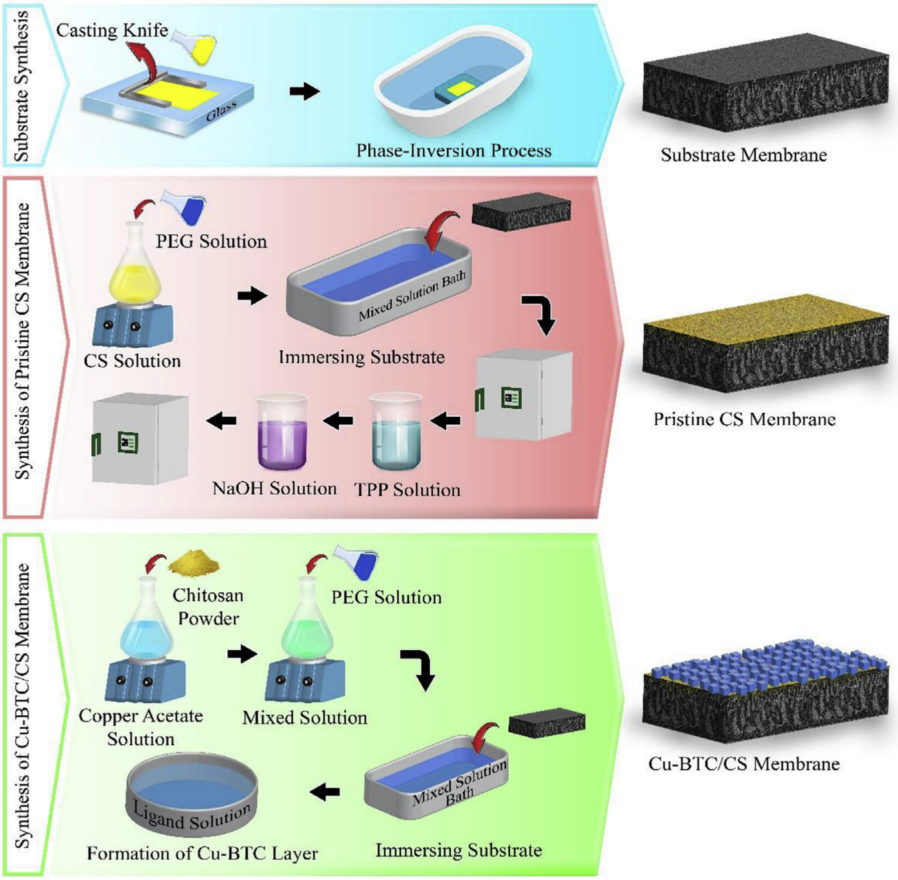

Fig. 1. Schematic of the membrane fabrication and modification procedures.

Coating [6], surface grafting [7], covalent immobilization [8–10], layer by layer assembly (LBL), and crosslinking [11,12] are the most frequently applied surface modification strategies. LBL is an efficient strategy for preparing modified multilayers on a membrane surface [12]. The number of multi-layers can be precisely controlled to form a uniform compact active layer with enhanced ions separation. LBL has been widely used for the growth of metal-organic frameworks (MOFs). It provides MOF uniform thin films with finely-tuned thicknesses, as it involves controlled sequential coating steps [13]. On account of their hybrid organic/inorganic structure, high surface area, and adjustable pore size, MOFs have emerged as promising porous materials for various separation applications [14]. Generally, the methods for MOF films formation can be divided into three classes: the direct growth approach using a solvothermal mother solution [15], the secondary seeding growth technique [16], and the interfacial assembly process [17,18]. Cu-BTC, a porous MOF produced by the coordination bonding between copper cations and benzene-1,3,5-tricarboxylate (BTC) as linker, is an appropriate candidate for preparation of thin films [19]. The Cu-BTC thin films can be fabricated on the surface via solvothermal [19], electrospraying [20], electrochemical [21], and interfacial synthesis methods [22].

In the seeding method, the nature of the substrate affects the MOFs formation. Several inorganic substrates, such as gold, silicon, alumina and fabrics, have been used for MOFs growth, while polymeric materials, such as silk and cotton, have been used rarely [23]. However, functional groups of polymeric substrates can serve as nucleation sites to accelerate the growth of MOFs [24], which have led to formation of advanced MOF-based nanocomposites. In the case of Cu-BTC, copper ions react with the substrate to introduce stable Cu^{2+} for subsequent nucleation [25]. The substrates with fixed negative charges appear to have strong interactions with the Cu^{2+} ions, facilitating the formation of Cu-BTC films [26]. In particular, the presence of –OH and –COOH functional groups on the substrate surface provides preferred sites for attachment of Cu-BTC clusters [26].

In this study, a novel membrane is prepared via rapid formation of Cu-BTC clusters on the PES membrane surface already coated with a chitosan (CS) layer. CS is a green and inexpensive biopolymer comprising amino and hydroxyl functional groups with excellent film-forming ability. A CS layer with high permeance is formed by dip-coating on the PES surface and then used as the seeding substrate for in-situ synthesis of Cu-BTC clusters. The performance of the Cu-BTC/CS membrane is studied in low-pressure NF, by investigating manganese and iron rejections, as well as water permeance. The morphology and physicochemical properties of the fabricated Cu-BTC/CS membrane are thoroughly evaluated by several analyses, and molecular dynamics (MD) is used to predict water molecules diffusivity in the thin film and the interaction energy between the Cu-BTC clusters and CS. Furthermore, the antimicrobial activity of the Cu-BTC/CS membrane against *E. coli* is assessed, and the antifouling property of the membranes are evaluated with organic and biological foulants.

2. Materials and methods

2.1. Materials

PES (Ultrason E6020P, $M_w = 58000\,g/mol$), *N,N*-dimethylformamide (DMF, Scharlau), and polyvinylpyrrolidone (PVP, with $M_w = 25000\,g/mol$, Merck) and Triton X-100 (Merck) were used to prepare the casting solution. CS (medium M_w, Orbital), sodium hydroxide (NaOH, Merck), acetic acid (glacial, Merck), sodium tripolyphosphate (TPP, Across), polyethylene glycol (PEG6000, Scharlau), copper acetate monohydrate ($Cu(CO_2CH_3)_2{\cdot}H_2O$, with $M_w = 199.65\,g/$

mol, Sigma-Aldrich), and 1,3,5-benzenetricarboxylic acid ($C_9H_6O_6$, Merck) were used for the preparation of the modified membrane. Manganese chloride ($MnCl_2{\cdot}4H_2O$), potassium permanganate ($KMnO_4$), and iron ammonium sulfate ($(NH_4)_2Fe(SO_4)_2{\cdot}6H_2O$) were supplied from Merck. Sodium alginate (Sigma-Aldrich), humic acid (Across), *Escherichia coli* (*E. coli*, ATCC 1399), potassium phosphate (KH_2PO_4, Merck), magnesium sulfate ($MgSO_4$, Merck), sodium chloride (NaCl, 99.5%, Merck), sodium bicarbonate ($NaCO_3$, Merck), ammonium chloride (NH_4Cl, Merck), and calcium chloride ($CaCl_2$, Merck) were used for synthesis of wastewater effluents.

2.2. Fabrication of thin membranes

The procedures used to fabricate of the membranes are schematically presented in Fig. 1. The substrate was obtained by conventional phase inversion induced by a non-solvent. The dope solution was obtained by dissolving 14% w/w PES, 2% w/w Triton X-100, and 1% w/w PVP in DMF. The layer of CS and the modified membranes were formed by dip coating in a CS solution and subsequently by in-situ synthesis of Cu-BTC, respectively.

2.2.1. CS coating on the PES substrate

To prepare the CS solution, 0.5 g CS was dissolved in aqueous acetic acid solution (75 mL, 2% v/v) under stirring for 1 h at 80 °C. The impurities were then removed by microfiltration. A solution consisting of 0.1 g PEG and 25 mL water was added to the CS solution, and the final solution was stirred at room temperature for 1 h. The CS/PES membrane was fabricated by immersing the PES substrate into the CS/PEG solution for 2 min. After that, the CS/PES membrane was heat treated in an oven at 80 °C for 15 min. After cooling the sample to room temperature, the membrane was soaked into a solution containing 0.2 g TPP and 100 mL water for 10 s. The cross-linked membrane was kept in an aqueous NaOH solution (2% v/v) for 30 min. Finally, the modified membrane was washed several times with water to eliminate the residual NaOH.

2.2.2. Cu-BTC/CS membrane fabrication

0.5 g of copper acetate was mixed in 75 mL of acetic acid solution (2% v/v) under sonication for 20 min. Then, 0.5 g of CS powder was dissolved under stirring at 80 °C for 1 h. Subsequently, 25 mL of aqueous solution containing 0.1 g PEG was also added to the mixture. After cooling to room temperature, the substrate was immersed in the solution and the excess solution was removed from the surface of the substrate. To obtain the Cu-BTC/CS membrane, the substrate surface was immersed in a solution containing 0.5 g of BTC and 100 mL of ethanol. Finally, the excess solution was eliminated from the membrane surface and the final membrane was placed in an oven at 80 °C for 1 h, before cooling to ambient temperature.

2.3. Membrane characterization

ATR-FTIR spectroscopy (Thermo Scientific, USA) was carried out to evaluate the chemical structure and the functional groups of the membranes surface. Roughness and surface topology of the membranes were analyzed using AFM (EasyScan II, Switzerland). The surface wettability of the membranes was investigated by contact angle measurement (G10, KRUSS, Germany). Chemical binding and elemental compositions of the selective layer were evaluated by XPS spectroscopy (Bestec, Germany). The surface charge of the membranes was determined by a zeta potential analyzer (Anton Paar USA, Ashland, VA). Cross sections and surface morphologies of the membranes were visualized by means of a FE-SEM (MIRA3 TESCAN) equipped with an energy-dispersive X-ray (EDX).

Effective mean pore size of the CS and Cu-BTC/CS membranes was calculated by gas permeation method via a home-made gas permeation cell [27]. The lab-scale experimental setup consisting of a gas reservoir, membrane cell, and a flowmeter was used to measure the surface pore size. The membrane sample was loaded into the cell and fixed with two O-rings at each side of membrane. While passing nitrogen through the membrane, the inlet and outlet pressures were recorded. The gas flow rates were determined by measuring the rise rate of a soap bubble in the flowmeter. Whereby, the effective mean surface pore size of the membranes was calculated by Eq. (1) [27]:

$$r_{p,m} = \frac{16B_r}{3A_r}\left(\frac{8RT}{\pi M}\right)^{0.5}\mu \tag{1a}$$

where $r_{P,m}$ is mean pore radius (m), and R, T, M, and μ are the gas constant ($R = 8.314\ J\ mol^{-1}K^{-1}$), the absolute temperature (K), the gas molecular weight (kg/mol), and the gas viscosity (Pa·s), respectively. Furthermore, the parameters A_r and B_r were determined, respectively, as intercept and slope of the curve describing the trend of the total gas permeance versus the mean pressure.

2.4. Simulation methods

All simulations were performed with Materials Studio 6 and COMPASS force field. 'Charge Qeq' was used to regulate the electrostatic charge of atoms. A geometry optimization was performed based on smart minimizer method and electrostatic interactions were considered by Ewald Summation Method (accuracy of 10^{-5} kcal/mol). The van der Waals interaction was computed with the atom based method (cutoff distance of 15 Å). Temperature and pressure were adjusted using Nose and Berendsen algorithms, respectively.

2.4.1. Construction of thin film membranes

The monomer of CS was first constructed by the 'Build Module' (Fig. 2a). Then, the homopolymer of CS including 65 monomers was made. The Cu-BTC clusters containing four BTC ligands with molecular weight of 963.624 g/mol were constructed as shown in Fig. 2b. The first simulation cell was generated by CS only and the second one was built by considering CS and three Cu-BTC clusters.

After geometry optimization and minimizing the energy of the structures, the simulation procedure was followed by running an NPT (the number of particles, temperature, and volume are constant) ensemble at 298.15 K and 100 kPa for 3 ns to attain equilibrium. After this step, the latest snapshot was selected to compute the interaction energies and diffusion coefficients. The simulated CS and Cu-BTC/CS nanocomposites are shown in Fig. 2c and d, respectively.

2.4.2. Computation of diffusion coefficients

To investigate the water transport properties of the membranes, water diffusion coefficients were obtained by a linear curve fitting of the mean-square displacement (MSD) diagram according to Einstein's relationship for diffusion [28]:

$$MSD(t) = \frac{1}{N}\sum_{i=1}^{N}\langle[r_i(t_0+t) - r_i(t_0)]^2\rangle = B + 6D.\,t \tag{1b}$$

where D is the molecular diffusion coefficient, B is a constant, N is the number of water molecules, and r_i is the vector of location in time t_0 and $t_0 + t$.

For the calculation, 20 molecules of water were loaded in each membrane simulation cell for both CS and Cu-BTC/CS membranes. MD simulations were used to simulate the water molecules diffusion into the structures. After a primary NPT run to attain a new equilibrium for 100 ps, the system was simulated by means of an NVT (number of particle, temperature, and volume are constant) ensemble at 298.15 K for 500 ps. Fig. 2e and f displays the water molecules loaded in CS and Cu-BTC/CS simulation cells, respectively.

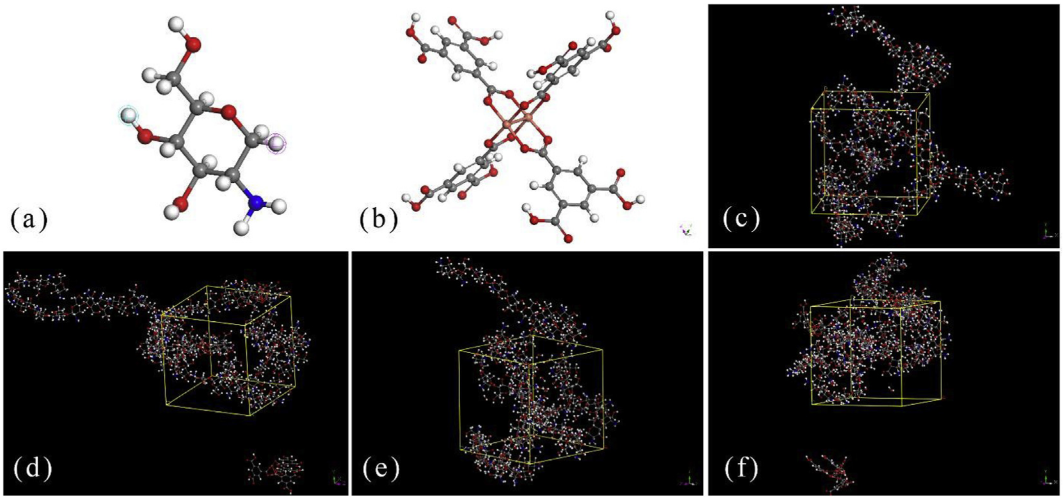

Fig. 2. Molecular structures of (a) the CS monomer and (b) a Cu-BTC cluster. Latest snapshots of the molecular configuration of the simulation cell after 3000 ps NPT MD simulations for: (c) CS, (d) Cu-BTC/CS composite, (e) CS with 20 loaded water molecules, and (f) Cu-BTC/CS with 20 loaded water molecules. The gray, blue, white, light salmon, and red spheres are carbon, nitrogen, hydrogen, copper, and oxygen atoms, respectively.

2.5. Fluorescence imaging

E. coli bacteria were cultivated in LB agar at 37 °C for 24 h and then a distinct colony was cultivated in 50 mL Terrific Broth (TB) while shaking at 150 rpm for 12 h at 37 °C. The resulting solution was then centrifuged at room temperature for 10 min followed by washing twice with PBS buffer to eliminate the residual TB. The stock sample of *E. coli* in PBS prepared with the cell density of ca. $(1.0 \pm 0.1) \times 10^7$ cells/mL. The membrane samples (1×1 cm^2) were contacted with 1 mL aliquot of the bacteria stock suspension for ca. 1 h. The remaining bacteria pellets were then removed using PBS buffer and the membranes were stained for 20 min in the dark at room temperature with the final concentrations of 20 µM of PI, and 5 µM of SYTO9. After removing the extra solution, images of the sames were taken. A Leica DMRXE microscope coupled with a digital image capture system (Tucsen model TC-3) was used to image the bacteria.

2.6. Membrane performance

A cross-flow filtration setup was applied to evaluate the productivity as well as the manganese and iron rejection of the membranes at 25 °C and 3 bar. The effective surface area of membrane and flow velocity were 30 cm^2 and 25 cm/s, respectively. The water flux (J) was calculated using:

$$J = \frac{V}{A \cdot \Delta t} \tag{2}$$

Where V is the permeate volume passed through the membrane (L) during the filtration time, Δt (h), and A is the effective area (m^2). A synthetic aqueous solution was used as feed solution, including 2% of Fe, 2% of Mn, and 2% of $KMnO_4$. The following equation was applied to calculate the rejection (R):

$$R\ (\%) = \left(1 - \frac{C_p}{C_f}\right) * 100 \tag{3}$$

where C_f and C_p are bulk feed and permeate concentrations of metal, respectively, measured by atomic absorption spectroscopy. All permeation experiments were performed three times and the average values are reported.

2.7. Membrane fouling Assessment

The antifouling properties of the membrane were evaluated by two foulant solutions containing 0.4 mM NaCl, 0.2 mM $NaHCO_3$, 0.3 mM $CaCl_2$, and humic acid (30 mg/L) or sodium alginate (250 mg/L) dissolved in DI water by using a cross-flow system at 25 °C and 3 bar, and at a cross-flow velocity of 12.5 cm/s.

For evaluation of biofouling propensity, the system was fumigated with a 70 wt% ethanol solution for 45 min before every test. To entirely remove the ethanol, the system was washed by deionized (DI) water several times. An aqueous solution containing 0.45 mM KH_2PO_4, 0.61 mM $MgSO_4$, 9.20 mM NaCl, 0.5 mM $NaHCO_3$, 0.93 mM NH_4Cl, and 0.5 mM $CaCl_2$ was applied as the synthetic wastewater. A desirable amount of bacterial culture was added to the solution at steady state to attain a primary concentration of $\sim 10^7$ CFU/L. The pure water flux of the cleaned membrane was measured under the same condition of the initial flux experiment, to obtain the flux recovery values.

3. Results and discussion

3.1. Film density and water diffusion coefficients from MD simulations

The upward trend of simulation cell density over a period of 3000 ps NPT run is shown in Fig. 3 for the CS and Cu-BTC/CS membranes. The density of the CS sample increases gradually to reach a steady-state, while the Cu-BTC/CS graph shows several incremental steps during the simulation time. When the species, i.e., Cu-BTC clusters and the

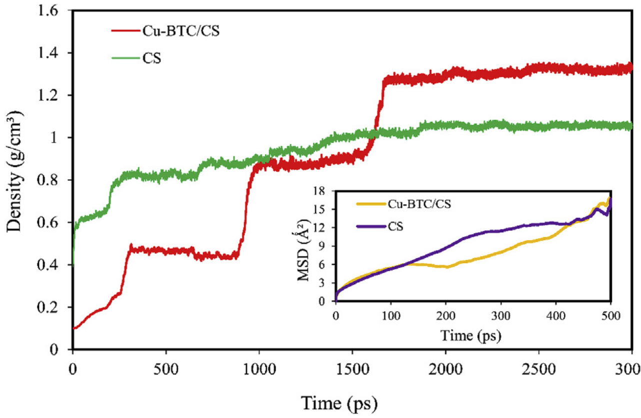

Fig. 3. Predicted densities of the CS and Cu-BTC/CS membranes vs. the simulation time. The inserted plot indicates the mean square displacement of water molecules.

Table 1
MD-predicted molecular weight of the polymer chain, density of thin films after 3 ns NPT run, and simulated diffusivity coefficients of water molecules in the thin films after 500 ps NVT run.

Sample	CS thin film	Cu-BTC/CS thin film
Polymer molecular weight (g/mol)	10477.2	10477.2
Simulation cell density (cm^3/g)	1.06	1.33
D (10^{-8}; cm^2/s)	42.8	39.3

polymer chains, approached to each other, the density enhances significantly due to the presence of attractive forces, resulting in a higher final value of the density for the Cu-BTC/CS layer. To investigate the transport of water molecules into the thin films and to determine the effect of Cu-BTC MOFs on the water diffusion coefficient, the mean-square displacement (MSD) of water molecules was calculated over 500 ps in a NVT run and the results are presented in the inset of Fig. 3. The MSD diagrams almost overlap, suggesting a similar value of water diffusion coefficients for the two samples.

The main features of the simulation cell, including the final density of the samples, the molecular weight of the polymer chain, and the diffusion coefficients are also provided in Table 1. The results obtained from the diffusion of water molecules in three directions in Cartesian coordinates are similar for the two films. Despite the fact that the nonporous Cu-BTC clusters increase the density of the thin film as well as its mass transfer resistance, the diffusion coefficient is not negatively affected thanks to the enhanced water affinity of the Cu-BTC-modified thin film.

The energy analysis illustrates that the total potential energy of Cu-BTC/CS nanocomposites dramatically dropped from −7278.6 to −13037.9 kcal/mol when 20 water molecules were loaded into the structure. In contrast, the total potential energy of the simulation cell related to CS alone slightly increased from 2435.2 to 2456.2 kcal/mol under similar conditions. The reduction of the energy level suggests more significant interactions between the membrane and water molecules, attributed to the presence of Cu-BTC clusters and especially that of the open metal sites in the Cu-BTC structure. The water-membrane interactions can enhance the membrane water affinity and consequently the water permeability of the layer. Also, the strong intermolecular interactions between Cu-BTC clusters and the CS chains can also reduce the structural defects of the polymeric composite, to form a more compact thin layer. This interaction was also determined from the results of the molecular dynamics simulation according to the following equation [29]:

$$E_{interaction} = E_{Composite} - (E_{Chitosan} + E_{Cu-BTC}) \tag{4}$$

where $E_{interaction}$, $E_{Composite}$, $E_{Chitosan}$, and $E_{Cu\text{-}BTC}$ are interaction energy, composite total energy, thin film total energy after removing Cu-BTC clusters, and thin film total energy after omission of CS, respectively. The complete results for these energy quantities are given in Table 2. The negative value of the $E_{interaction}$ indicates that the energy level of the composite is lower than the sum of the energy of different species at steady state. This result verifies the formation of a stable structure and proves strong interactions between CS chains and Cu-BTC clusters.

3.2. Properties of pristine CS and Cu-BTC/CS membranes

ATR-FTIR spectroscopy was conducted to investigate the functional groups of both pristine CS and Cu-BTC/CS membranes (Fig. 4). The bands at 1150 and 1300 cm^{-1} are related to symmetric and asymmetric O=S=O stretching vibrations of the PES support, respectively. The peak at 1240 cm^{-1} can also be assigned to the asymmetric C–O–C stretching vibration of the PES substrate [30]. The characteristic infrared peaks appearing at 1581 cm^{-1} 1651 cm^{-1} are assigned to the vibration of N–H bending and vibration of C–N stretching in primary amide (amino group), and to the vibration of C=O stretching in secondary amide (–NHCO–) CS membrane, respectively [31]. The wide peak observed in the range 3100–3400 cm^{-1} is assigned to hydrogen bonds of the hydroxyl groups of CS [32]. The peak at 1150 cm^{-1} represents vibration of P=O stretching owing to cross-linking the CS chains with TPP [33]. Two peaks at 1360 and 1430 cm^{-1} are related to carboxylate symmetric stretch, while the carboxylate asymmetric stretch peak appeared at 1610 cm^{-1} [34]. The other peaks including 714, 832, and 1100 cm^{-1} indicate C–C ring out-of-plane bending, C–H out-of-plane, and C–H in-plane bending vibrations, respectively [35]. As can be seen, the intensity of the primary and secondary amides, and hydroxyl group peaks in Cu-BTC/CS membrane is lower compared to the pristine CS membrane corroborating the attachment of copper atoms to the CS chains.

Table 2
Energy quantities (kcal/mol) of the components calculated with MD.

Sample	$E_{Composite}$	$E_{Chitosan}$	$E_{Cu\text{-}BTC}$	$E_{Intraction}$
Cu-BTC/CS	−7278.65	2830.49	−8898.52	−1210.62

AFM analysis was performed to characterize the roughness of pristine CS and Cu-BTC modified CS membranes. Fig. 5a and b shows two dimensional (2D) and 3D AFM images, respectively, and Table 3 lists the values of roughness parameters of the membranes including average roughness (R_a) and root mean squared roughness (R_{rms}). The pristine CS membrane showed relatively smooth surface (average roughness of 9.4 nm), while the Cu-BTC/CS membrane demonstrated higher surface roughness (average roughness of 35.1 nm). This increase in the surface roughness can be attributed to the presence of a thin layer of Cu-BTC clusters [36]. As depicted in Fig. 5, the contact angle reduced after the formation of Cu-BTC on the surface, indicating higher wettability of the modified membrane. The improved wettability of the membrane is ascribed to formation of the stable structure of the Cu-BTC clusters and strong interactions between the clusters and the CS chains as discussed earlier in the MD simulations section. These surface properties are expected to decrease the foulant deposition propensity. In addition, the surface pore size of the membranes was measured using gas permeation test and the obtained results are given in Table 3. The surface pore size decreased from around 22 nm to around 13 nm after Cu-BTC deposition.

FE-SEM was applied to visualize the membrane morphology. Fig. 6a–d illustrate the surface and cross-sectional micrographs of the pristine CS/PES and Cu-BTC/CS/PES membranes. The pristine CS/PES membrane presented a smooth surface with asymmetric structure composed of a dense ultra-thin layer of well-coated CS on the surface of the PES substrate (Fig. 6a). Indeed, after soaking in CS solution a dense layer with a thickness of about 210 nm forms on the PES support layer (Fig. 6b). However, a ridge-and-valley structure was created upon anchoring the Cu-BTC clusters on the active sites (amine and hydroxyl groups) of the CS membrane (Fig. 6c). Following the deposition of Cu-BTC clusters on the CS coated PES membrane, a thin layer with a thickness of about 240 nm formed. Furthermore, appearance of the copper peak in the EDX spectrum of the Cu-BTC/CS membrane (illustrated in Fig. 6f) confirms the successful formation of Cu-BTC clusters on the CS layer.

To gain a better understanding of the elemental compositions and chemical bonds of the pristine CS and Cu-BTC/CS membranes, the surface of the membranes was analyzed using XPS analysis. As depicted in Fig. 7, the XPS survey demonstrates that the surface of both membranes contains carbon, nitrogen, and oxygen atoms. Additionally, the Cu-BTC/CS membrane spectrum presented a peak of copper, Cu (2p 3/2), which is located at around 934.14 eV [37]. Table 4 presents the elemental compositions and O/N ratio of the CS and Cu-BTC/CS membranes. The Cu-BTC/CS membrane has a higher oxygen and a lower nitrogen percentages and hence higher O/N ratio than the pristine CS membrane. This significantly higher O/N ratio is attributed to

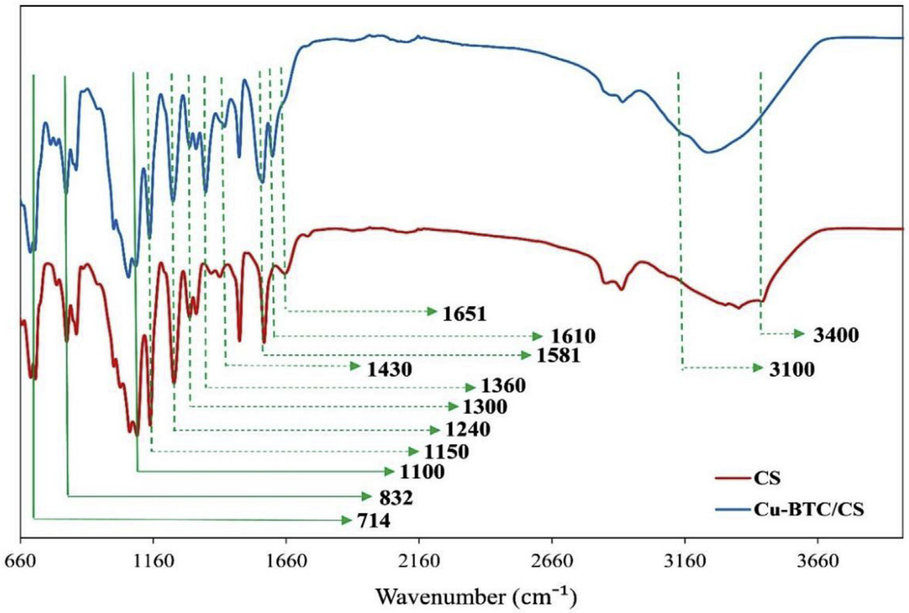

Fig. 4. ATR-FTIR spectra of the pristine CS and Cu-BTC/CS membranes on PES supports.

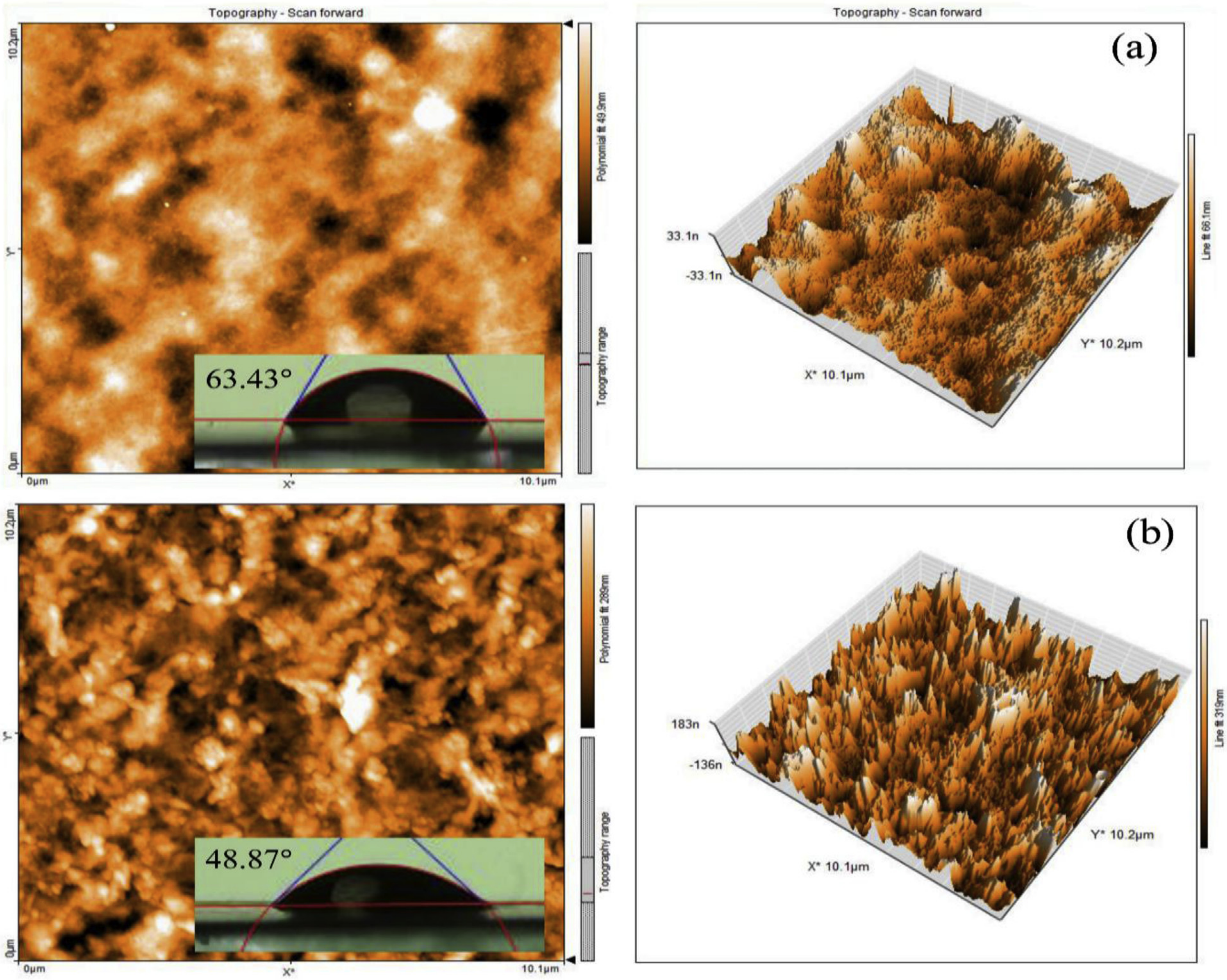

Fig. 5. AFM images of the (a) pristine CS and (b) Cu-BTC/CS membranes. The inserted images are the water contact angle photos of the CS and Cu-BTC/CS membranes.

Table 3
Roughness and surface pore size values of the membranes.

Membrane type	Roughness parameters (nm)		mean surface pore diameter (nm)
	average roughness (R_a)	root mean squared roughness (R_{rms})	
CS membrane	9.4	11.4	21.7 ± 2.1
Cu-BTC/CS membrane	35.1	43.9	13.3 ± 1.8

the presence of Cu-BTC MOFs with abundant oxygen-containing functional groups. Moreover, the increased O/N ratio may be considered as an indicator of the chelation effect of Cu^{2+} ions with the hydroxyl and amine groups of the CS. The chelation decreases the penetration of the BTC ligands into the CS layer [38].

Further information on the chemical structure of the membranes can be obtained by the deconvolution of the C (1s) high resolution spectra, as presented in Fig. 7b and d. The spectra include three peaks: a major peak located at 285 eV attributed to C−C/C=C bonds [39], an intermediate peak appeared at 286.5 eV ascribed to C−N bond, and a minor peak at 288.5 eV corresponded to amides O=C−N and O=C−O bonds [39]. Moreover, the appearance of a Cu2p3/2 peak at 934.14 eV and its two additional shake-up satellite peaks at 941.87 and 944.32 eV confirms that Cu in the MOF synthesized has divalent nature.

Zeta potential measurements were applied to evaluate the surface charge of the CS and Cu-BTC/CS membranes (Fig. 8). Negative surface charges were observed for both membranes. The surface amine groups on the of the pristine CS membrane start to protonate at roughly pH 6 and result in a lower density of negative charges for slightly acidic pH values. Larger values of negative zeta potential were observed after formation of Cu-BTC clusters, corresponding to the deprotonation of carboxyl functional groups in the MOFs structures [40]. Since the bacterial cells (*E. coli*) are generally negatively charged in a pH range 4–9 [41], this potential may provide an electrostatic repulsion to bacteria attachment and a decrease in their deposition, resulting in lower biofouling tendency.

3.3. Separation performance of pristine CS and of Cu-BTC/CS membranes

The results of water flux, iron and manganese removal for both the CS and Cu-BTC/CS membranes are presented in Fig. 9. The water flux of Cu-BTC/CS membrane ($44\,L\,m^{-2}h^{-1}$) is higher than that of pristine CS membrane ($39\,L\,m^{-2}h^{-1}$). The higher flux for Cu-BTC/CS membrane can be assigned to its surface wettability. Although the formation of a Cu-BTC/CS thin film increases the mass transfer resistance, the high water affinity of the Cu-BTC/CS membrane, verified by the measured contact angle and MD simulations, facilitate partitioning and permeation of the water molecules [42]. Often the membrane permeance decreases after surface modification by creation of an additional coating, due to the mass transfer resistance of this additional layer. In this study, however, a slight increase in water flux was observed, thanks to the high water affinity of Cu-BTS clusters and enhanced surface wettability. In addition, the Cu-BTC/CS membrane exhibited higher manganese and

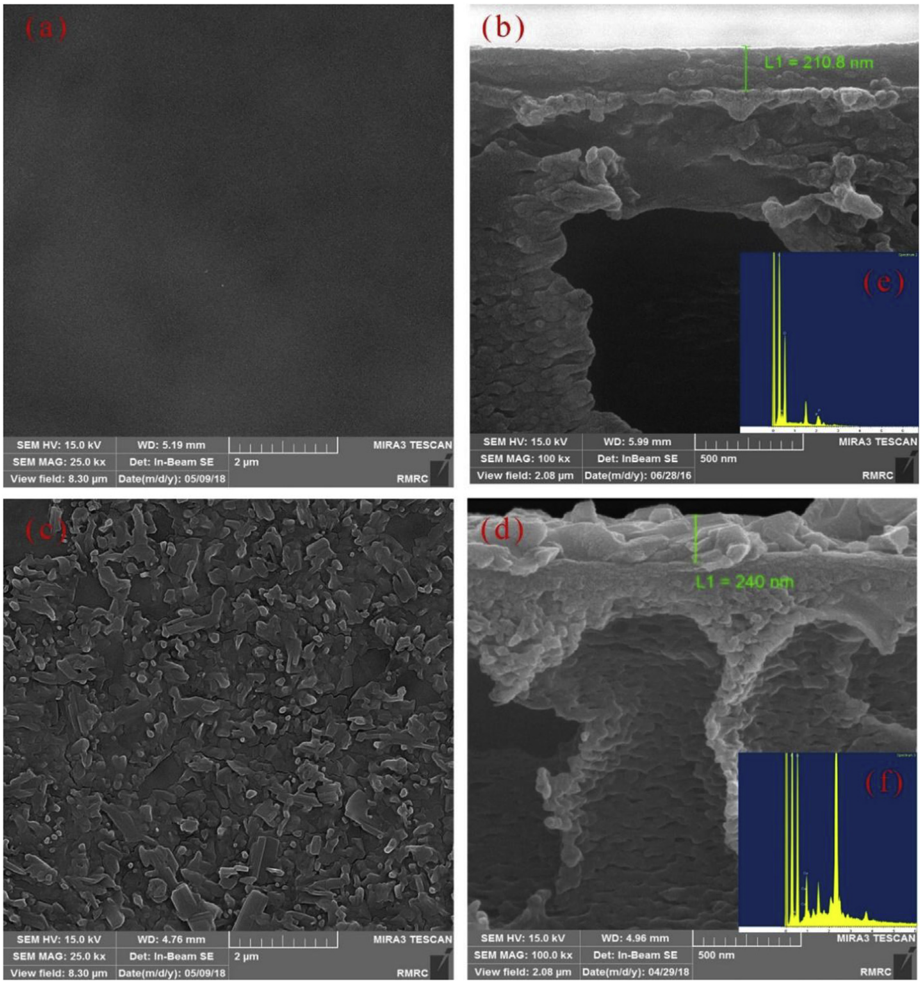

Fig. 6. Surface and cross-sectional FE-SEM micrographs of the pristine CS/PES and Cu-BTC/CS/PES membranes: (a, b) pristine CS/PES membrane and (c, d) Cu-BTC/CS/PES membrane. EDX analysis of (e) the CS/PES and (f) Cu-BTC/CS/PES membranes.

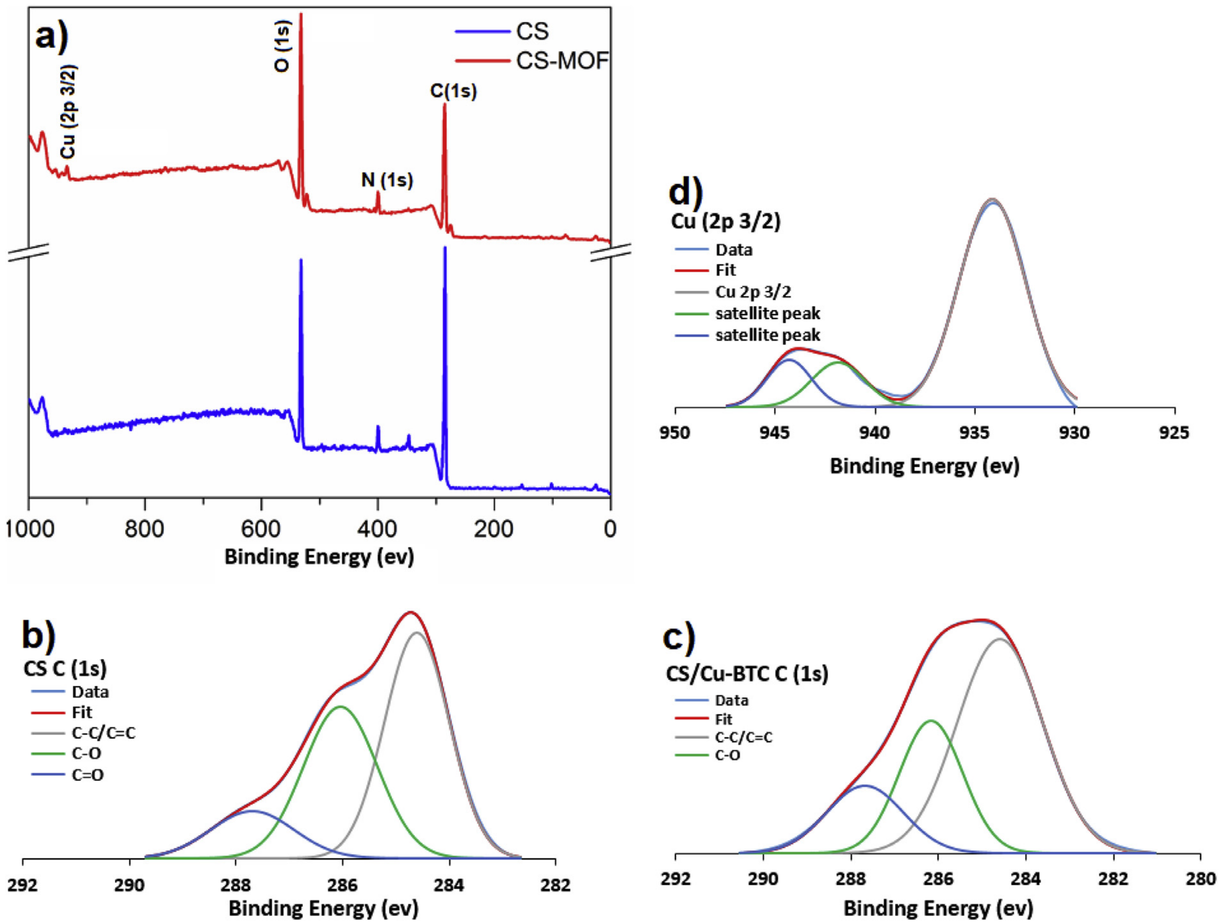

Fig. 7. (a) XPS survey spectra of the CS and Cu-BTC/CS membranes, (b, c) high-resolution XPS spectra of C (1s) of the CS and Cu-BTC/CS membranes, and (d) Cu (2p 3/2) of the Cu-BTC/CS membrane.

Table 4
Elemental compositions and O/N ratio of the CS and Cu-BTC/CS membranes.

Membrane	Atomic concentration (%)				O/N ratio
	C (1s)	O (1s)	N (1s)	Cu (2p)	
CS membrane	75.3	21.13	3.57	–	5.92
Cu-BTC/CS membrane	66.02	30.45	3.25	0.27	9.37

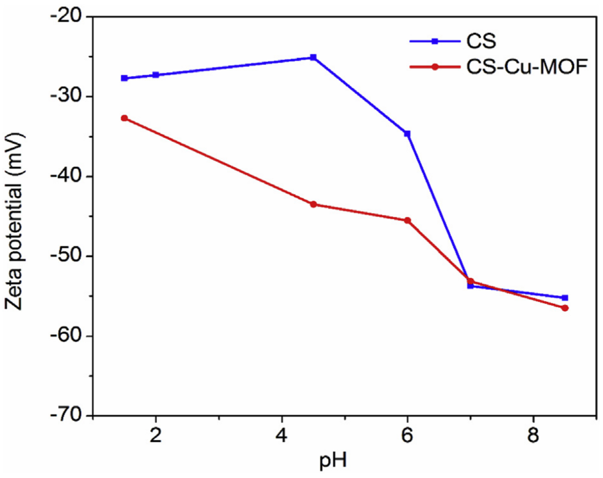

Fig. 8. Zeta potentials of the pristine CS and Cu-BTC/CS membranes.

iron removal compared to the pristine CS membrane. The observed rejection for Cu-BTC/CS membranes was 86% and 99% for Mn and Fe, respectively. The formation of a Cu-BTC/CS film increased the density of the active layer, which enhanced the resistance to mass transport and led to better metal removal by preventing metal ions transport by zigzag passage [43].

The performance of other loose nanofiltration nanocomposite membranes reported in the literature for metal removal is summarized in Table 5. The Cu-BTC/CS membrane developed in this study possessed a competitive performance in removing Mn and Fe ions compared to the existing membranes.

3.4. Antibacterial activity

Antibacterial activity of the pristine CS and Cu-BTC/CS membranes was assessed by live and dead staining visualized by a fluorescence microscopy. Fig. 10 presents representative images of the membranes after exposing with a bacterial solution, indicating a significant reduction in the number of live bacteria on the surface of the Cu-BTC/CS membrane. The Cu-BTC/CS membrane demonstrated over 83% antibacterial activity against *E. coli* in comparison to 47% of the pristine CS membrane. As antibacterial properties of the CS were previously proven [57], a number of dead bacteria is also observed on the surface of the CS membrane. However, the improved antimicrobial activity of the CS/Cu-BTC membrane is attributed to the synergetic effect of the CS layer and Cu-BTC clusters, providing higher accessible active sites that resulted in higher toxicity toward bacterial inactivation. Antifungal properties against *Saccharomyces cerevisiae* and antibacterial properties

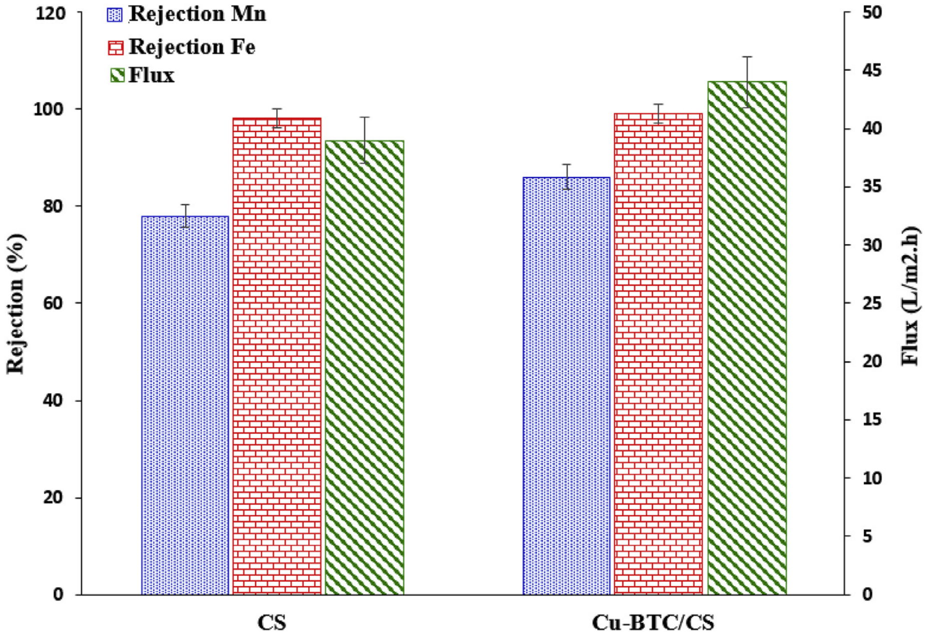

Fig. 9. Rejection and water flux of the CS and Cu-BTC/CS membranes.

against the *E. coli* (Gram-negative) and *S. aureus* (Gram-positive) have been reported for Cu-BTC-containing materials [57]. Cu-BTC MOFs are the reservoir of copper (Cu^{2+}) ions that can provide sustained antibacterial activity [58]. The proposed antibacterial mechanism includes the cell wall rupture and plasma membrane deterioration through contact with the Cu^{2+} metal sites, that can oxidize organic species [58].

3.5. Preliminary Assessment of bacteria and organic fouling of the membranes

Fig. 11a and b shows the trend of normalized water flux during the filtration of solutions containing biological and organic foulants, respectively. The water flux decreased remarkably in the beginning of the

Table 5
Heavy metals removal performance of various nano-composite membranes reported in the literature.

Membrane type	Metal ion	Process condition		Removal (%)/adsorption capacity (mg/g)	Ref.
		pH	T (°C)		
Poly ethylene oxide/chitosan nanofiber membrane	Pb (II)	5.5	25	Maximum adsorption capacity of: 237.2	[44]
	Cd (II)	5		248.1	
	Ni (II)	5		357.1	
	Cu (II)	6		310.2	
Chitosan/hydroxyl apatite composite membrane	Pb (II)	–	25–45	Maximum adsorption capacity of: 296.7	[45]
	Ni (II)			213.8	
	Co (II)			180.2	
Chitosan/TiO_2 nanofiber membrane	Cu(II)	2–7	25–45	Maximum adsorption capacity of: 90	[46]
	Pb (II)			75	
Chitosan/polycarbonate composite membrane	Cu (II)	–	–	Maximum adsorption capacity of: 5.9	[47]
Cellulose acetate UF	Mn	–	–	80% Rejection	[48]
Commercial nanofiltration membrane (NF270)	Mn (II)	2.35	22–25	75% Rejection	[49]
Microporous chitosan-PEG blend membrane	Mn (II)	9	27	Maximum adsorption capacity of: 16	[50]
	Fe (III)			38	
Chitosan/poly(ethylene oxide)/activated carbon nanofibrous membrane	Cr (VI)	1–6	25	Maximum adsorption capacity of: 261.1	[51]
	Fe (III)			217.4	
	Cu (II)			195.3	
	Zn (II)			186.2	
	Pb (II)			176.9	
Chitosan/hydroxymethyl cellulose composite membrane	Ni (II)	5.4	25	77% Rejection	[52]
Composite Graphene oxide/chitosan nanoplates incorporated into Polyethersulfone	Cr (VI)	–	–	89% Rejection	[53]
Chitosan/poly(vinyl alcohol)/zeolite electrospun composite nanofibrous membrane	Cr (VI)	7	25	98% Rejection	[54]
	Fe (III)			96% Rejection	
	Ni (II)			93% Rejection	
Fe_3O_4-NH_2 nanocomposite filled chitosan/poly(vinyl alcohol)/Polyethersulfone dual layers nanofibrous membrane	Cr (VI)	2–7	30–50	Maximum adsorption capacity of: 38	[55]
	Pb (II)			40	
Sulfated chitosan/poly(vinyl alcohol) membrane	Ni (II)	2–6	25–55	30% Rejection	[56]
	Cu (II)			70% Rejection	
CS/Cu-BTC membrane	Fe (III)	7	25	99% Rejection	This study
	Mn (II)			85% Rejection	

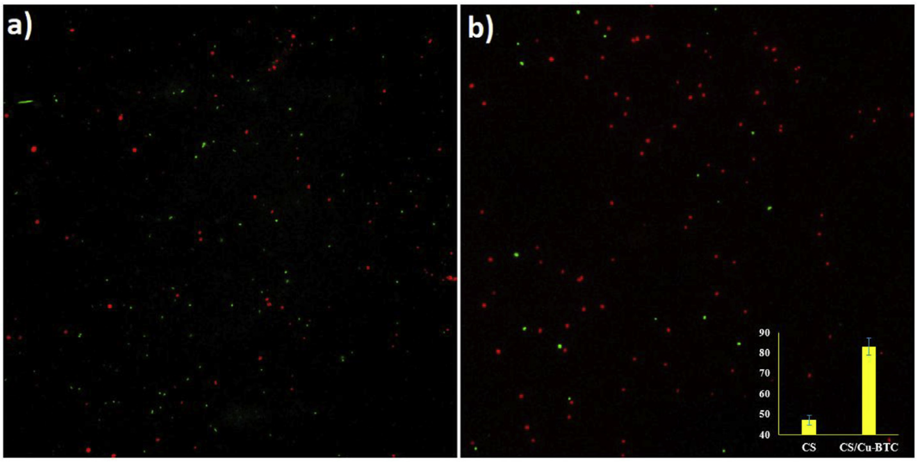

Fig. 10. Fluorescence images of *E. coli* cell pellets on the surface of (a) pristine CS and (b) Cu-BTC/CS membranes stained with SYTO 9 (green for live bacteria), and PI (red for dead bacteria).

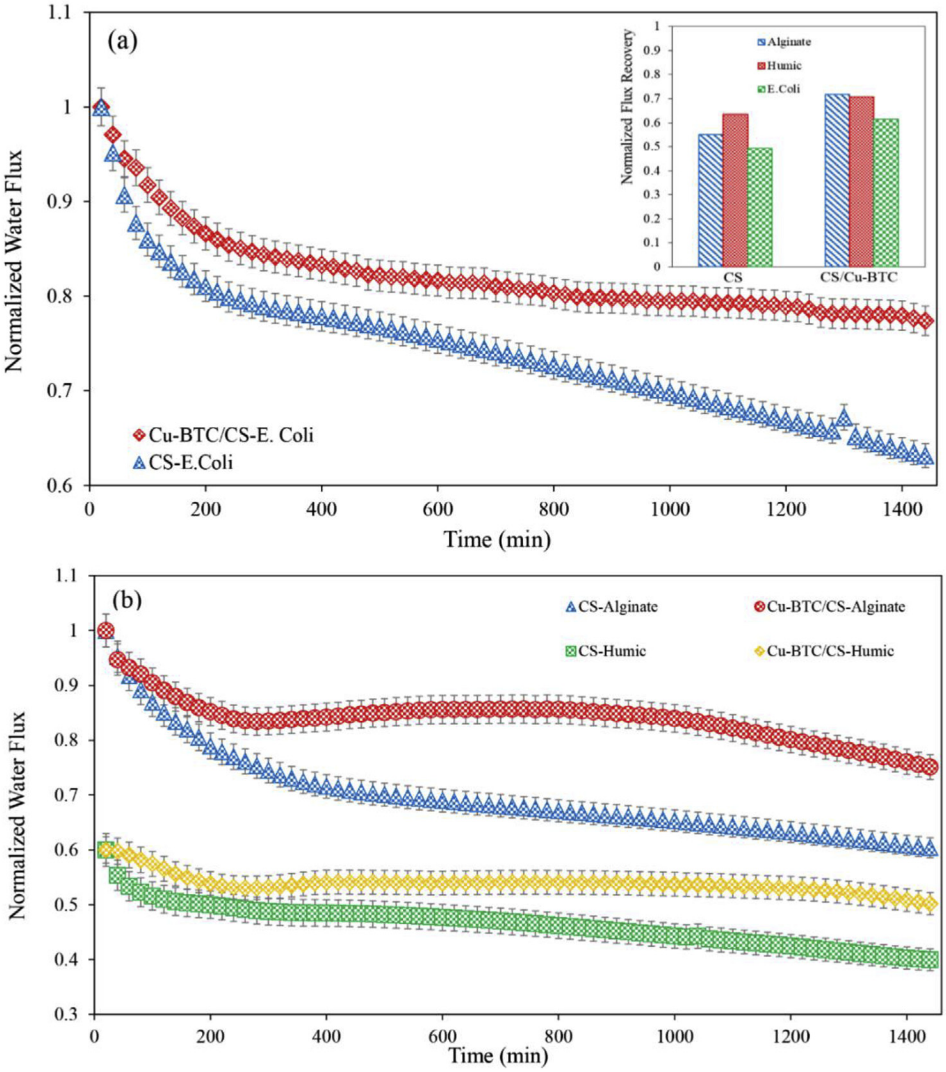

Fig. 11. Fouling performance of the pristine CS and Cu-BTC/CS membranes with the (a) bio-foulant and (b) organic foulant. The inserted bar chart displays the flux recovery.

experiments and then gradually declined over time. The Cu-BTC/CS membrane showed smaller reduction in the water flux (about 23%) due to biofouling resistance compared to CS membranes (about 37%), as shown in Fig. 11a. Compared to CS membrane, the enhanced antibiofouling properties of the Cu-BTC membrane can be ascribed to the combination of its higher surface wettability and stronger antibacterial activity reducing deposition and inactivating the cells [58]. Similarly, the results of organic fouling tests demonstrated that the Cu-BTC/CS membrane had a lower tendency to deposition of foulant molecules, lower water flux reduction, and better flux recovery than those of the pristine CS membrane. The improved fouling resistance of the MOF-containing membrane resulted from its higher surface wettability and lower propensity of organic matter to adhere to the membrane surface. Water molecules can easily adhere to a hydrophilic surface via hydrogen bonding and reduce foulant deposition, resulting in a greater antifouling resistance. The flux recovery improved from 55% to 71% (alginate as foulant) and from 61% to 70% (humic acid as foulant) by coating the CS membrane with a Cu-BTC film.

4. Conclusions

A new loose NF membrane was synthesized by a fast and facile in-situ deposition of a thin film of Cu-BTC MOFs over a CS/PES membrane. The presence of Cu-BTC clusters not only improved the productivity of the membrane, but also enhanced the Mn and Fe rejection. Moreover, MD simulations verified the formation of a stable structure and high compatibility of the Cu-BTC clusters with the CS layer, allowing for tuning the membrane properties and improving its separation performance. Successful formation of the Cu-BTC film on the surface of CS layer resulted in a more wettable surface, in turn translating into a reduction of the detrimental effects of organic fouling. In addition to better water affinity, stronger biocidal activity of the MOF layer led to excellent resistance of the Cu-BTC/CS membrane against bio-foulants. This work proposes a simple fabrication procedure, involving fast formation of the MOF clusters, thus offering a practical strategy for preparing membranes with favorable antifouling properties for the efficient removal of heavy metals from drinking water.

Acknowledgment

The authors acknowledge Babol Noshirvani University of Technology for financial support of this project (BNUT/925150005/94 and BNUT/4-6130593/97). The authors are also grateful for the research collaboration between Babol Noshirvani University of Technology, Politecnico di Torino, Drexel University, and the University of Alabama.

References

[1] J. Lin, C.Y. Tang, C. Huang, Y.P. Tang, W. Ye, J. Li, J. Shen, R. Van den Broeck, J. Van Impe, A. Volodin, A comprehensive physico-chemical characterization of superhydrophilic loose nanofiltration membranes, J. Membr. Sci. 501 (2016) 1–14.
[2] M.R. Esfahani, N. Koutahzadeh, A.R. Esfahani, M.D. Firouzjaei, B. Anderson, L. Peck, A novel gold nanocomposite membrane with enhanced permeation, rejection and self-cleaning ability, J. Membr. Sci. 573 (2019) 309–319.
[3] J. Zhu, Y. Zhang, M. Tian, J. Liu, Fabrication of a mixed matrix membrane with in situ synthesized quaternized polyethylenimine nanoparticles for dye purification and reuse, ACS.
[4] J. Zhu, N. Guo, Y. Zhang, L. Yu, J. Liu, Preparation and characterization of negatively charged PES nanofiltration membrane by blending with halloysite nanotubes grafted with poly (sodium 4-styrenesulfonate) via surface-initiated ATRP, J. Membr. Sci. 465 (2014) 91–99.
[5] M.R. Esfahani, S.A. Aktij, Z. Dabaghian, M.D. Firouzjaei, A. Rahimpour, J. Eke, I.C. Escobar, M. Abolhassani, L.F. Greenlee, A.R. Esfahani, Nanocomposite membranes for water separation and purification: fabrication, modification, and applications, Sep. Purif. Tech (2018).
[6] T. He, M. Frank, M. Mulder, M. Wessling, Preparation and characterization of nanofiltration membranes by coating polyethersulfone hollow fibers with sulfonated poly (ether ether ketone)(SPEEK), J. Membr. Sci. 307 (2008) 62–72.
[7] F. Liu, B.-r. Ma, D. Zhou, L.-J. Zhu, Y.-Y. Fu, L.-x. Xue, Positively charged loose nanofiltration membrane grafted by diallyl dimethyl ammonium chloride (DADMAC) via UV for salt and dye removal, React. Funct. Polym. 86 (2015) 191–198.
[8] S.F. Seyedpour, A. Rahimpour, G. Najafpour, Facile in-situ assembly of silver-based MOFs to surface functionalization of TFC membrane: a novel approach toward long-lasting biofouling mitigation, J. Membr. Sci. 573 (2019) 257–269.
[9] S.F. Seyedpour, A. Rahimpour, A.A. Shamsabadi, M. Soroush, Improved performance and antifouling properties of thin-film composite polyamide membranes modified with nano-sized bactericidal graphene quantum dots for forward osmosis, Chem. Eng. Res. Des. 139 (2018) 321–334.
[10] M.D. Firouzjaei, A.A. Shamsabadi, S.A. Aktij, S.F. Seyedpour, M. Sharifian Gh, A. Rahimpour, M.R. Esfahani, M. Ulbricht, M. Soroush, Exploiting synergetic effects of graphene oxide and a silver-based metal–organic framework to enhance antifouling and anti-biofouling properties of thin-film nanocomposite membranes, ACS Appl. Mater. Interfaces 10 (2018) 42967–42978.
[11] Q. Chen, P. Yu, W. Huang, S. Yu, M. Liu, C. Gao, High-flux composite hollow fiber nanofiltration membranes fabricated through layer-by-layer deposition of oppositely charged crosslinked polyelectrolytes for dye removal, J Memb. Sci. 492 (2015) 312–321.
[12] S. Rajesh, Y. Yan, H.-C. Chang, H. Gao, W.A. Phillip, Mixed mosaic membranes prepared by layer-by-layer assembly for ionic separations, ACS Nano 8 (2014) 12338–12345.
[13] K. Otsubo, T. Haraguchi, O. Sakata, A. Fujiwara, H. Kitagawa, Step-by-step fabrication of a highly oriented crystalline three-dimensional pillared-layer-type metal–organic framework thin film confirmed by synchrotron x-ray diffraction, J. Am. Chem. Soc. 134 (2012) 9605–9608.
[14] O. Shekhah, J. Liu, R. Fischer, C. Wöll, MOF thin films: existing and future applications, Chem. Soc. Rev. 40 (2011) 1081–1106.
[15] M.D. Firouzjaei, A.A. Shamsabadi, M. Sharifian Gh, A. Rahimpour, M. Soroush, A novel nanocomposite with superior antibacterial activity: a silver-based metal organic framework embellished with graphene oxide, Adv. Mater. Interf. 5 (2018) 1701365.
[16] F. Zhang, X. Zou, X. Gao, S. Fan, F. Sun, H. Ren, G. Zhu, Hydrogen selective NH2-MIL-53 (Al) MOF membranes with high permeability, Adv. Funct. Mater. 22 (2012) 3583–3590.
[17] R. Ameloot, F. Vermoortele, W. Vanhove, M.B. Roeffaers, B.F. Sels, D.E. De Vos, Interfacial synthesis of hollow metal–organic framework capsules demonstrating selective permeability, Nat. Chem. 3 (2011) 382.
[18] J. Liu, F. Sun, F. Zhang, Z. Wang, R. Zhang, C. Wang, S. Qiu, In situ growth of continuous thin metal–organic framework film for capacitive humidity sensing, J. Mater. Chem. 21 (2011) 3775–3778.
[19] S. Kayaert, S. Bajpe, K. Masschaele, E. Breynaert, C.E. Kirschhock, J.A. Martens, Direct growth of Keggin polyoxometalates incorporated copper 1, 3, 5-benzenetricarboxylate metal organic framework films on a copper metal substrate, Thin Solid Films 519 (2011) 5437–5440.
[20] A.H. Khoshaman, B. Bahreyni, Application of metal organic framework crystals for sensing of volatile organic gases, Sensor. Actuator. B Chem. 162 (2012) 114–119.
[21] R. Ameloot, L. Stappers, J. Fransaer, L. Alaerts, B.F. Sels, D.E. De Vos, Patterned growth of metal-organic framework coatings by electrochemical synthesis, Chem. Mater. 21 (2009) 2580–2582.
[22] J. Campbell, R. Davies, D.C. Braddock, A. Livingston, Improving the permeance of hybrid polymer/metal–organic framework (MOF) membranes for organic solvent nanofiltration (OSN)–development of MOF thin films via interfacial synthesis, J. Mater. Chem. A 3 (2015) 9668–9674.
[23] D. Kim, A. Coskun, Graphene oxide-templated preferential growth of continuous MOF thin films, CrystEngComm 18 (2016) 4013–4017.
[24] P.C. Lemaire, J. Zhao, P.S. Williams, H.J. Walls, S.D. Shepherd, M.D. Losego, G.W. Peterson, G.N. Parsons, Copper benzenetricarboxylate metal–organic framework nucleation mechanisms on metal oxide powders and thin films formed by atomic layer deposition, ACS Appl. Mater. Interfaces 8 (2016) 9514–9522.
[25] O. Shekhah, H. Wang, S. Kowarik, F. Schreiber, M. Paulus, M. Tolan, C. Sternemann, F. Evers, D. Zacher, R.A. Fischer, Step-by-step route for the synthesis of metal− organic frameworks, J. Am. Chem. Soc. 129 (2007) 15118–15119.
[26] D. Zacher, A. Baunemann, S. Hermes, R.A. Fischer, Deposition of microcrystalline [Cu 3 (btc) 2] and [Zn 2 (bdc) 2 (dabco)] at alumina and silica surfaces modified with patterned self assembled organic monolayers: evidence of surface selective and oriented growth, J. Mater. Chem. 17 (2007) 2785–2792.
[27] M. Mozafari, R. Abedini, A. Rahimpour, Zr-MOFs incorporated thin film nanocomposite-Pebax 1657 membranes dip coated on polymethylpentyne layer for efficient separation of CO_2/CH_4, J. Mater. Chem. A 6 (2018) 12380–12392.
[28] S. Mokhtari, A. Rahimpour, A.A. Shamsabadi, S. Habibzadeh, M. Soroush, Enhancing performance and surface antifouling properties of polysulfone ultrafiltration membranes with salicylate-alumoxane nanoparticles, Appl. Surf. Sci. 393 (2017) 93–102.
[29] A. Rahimpour, S.F. Seyedpour, S. Aghapour Aktij, M. Dadashi Firouzjaei, A. Zirehpour, A. Arabi Shamsabadi, S. Khoshhal Salestan, M. Jabbari, M. Soroush, Simultaneous improvement of antimicrobial, antifouling, and transport properties of forward osmosis membranes with immobilized highly-compatible polyrhodanine nanoparticles, Environ. Sci. Technol. 52 (2018) 5246–5258.
[30] W. Fu, C. Carbrello, X. Wu, W. Zhang, Visualizing and quantifying the nanoscale hydrophobicity and chemical distribution of surface modified polyethersulfone (PES) membranes, Nanoscale 9 (2017) 15550–15557.
[31] M. Li, Y. Wang, Q. Liu, Q. Li, Y. Cheng, Y. Zheng, T. Xi, S. Wei, In situ synthesis and biocompatibility of nano hydroxyapatite on pristine and chitosan functionalized graphene oxide, J. Mater. Chem. B 1 (2013) 475–484.
[32] M. Kumar, B.P. Tripathi, V.K. Shahi, Crosslinked chitosan/polyvinyl alcohol blend beads for removal and recovery of Cd (II) from wastewater, J. Hazard Mater. 172

(2009) 1041–1048.

[33] E. Costa, S. Silva, S. Vicente, C. Neto, P. Castro, M. Veiga, R. Madureira, F. Tavaria, M. Pintado, Chitosan nanoparticles as alternative anti-staphylococci agents: bactericidal, antibiofilm and antiadhesive effects, Mater. Sci. Eng. C 79 (2017) 221–226.

[34] H. Sun, X. Han, K. Liu, B. Shen, J. Liu, D. Wu, X. Shi, Metal-modified Cu-BTC acid for highly enhanced adsorption of organosulfur species, Ind. Eng. Chem. Res. 56 (2017) 9541–9550.

[35] J.B. DeCoste, G.W. Peterson, B.J. Schindler, K.L. Killops, M.A. Browe, J.J. Mahle, The effect of water adsorption on the structure of the carboxylate containing metal–organic frameworks Cu-BTC, Mg-MOF-74, and UiO-66, J. Mater. Chem. A 1 (2013) 11922–11932.

[36] A. Zirehpour, A. Rahimpour, S. Khoshhal, M.D. Firouzjaei, A.A. Ghoreyshi, The impact of MOF feasibility to improve the desalination performance and antifouling properties of FO membranes, RSC Adv. 6 (2016) 70174–70185.

[37] R.S. Kumar, S.S. Kumar, M.A. Kulandainathan, Efficient electrosynthesis of highly active Cu3 (BTC) 2-MOF and its catalytic application to chemical reduction, Microporous Mesoporous Mater. 168 (2013) 57–64.

[38] M.E. Ali, F.M. Hassan, X. Feng, Improving the performance of TFC membranes via chelation and surface reaction: applications in water desalination, J. Mater. Chem. A 4 (2016) 6620–6629.

[39] C.Y. Tang, Y.-N. Kwon, J.O. Leckie, Probing the nano-and micro-scales of reverse osmosis membranes—a comprehensive characterization of physiochemical properties of uncoated and coated membranes by XPS, TEM, ATR-FTIR, and streaming potential measurements, J. Membr. Sci. 287 (2007) 146–156.

[40] O. Coronell, B.J. Mariñas, X. Zhang, D.G. Cahill, Quantification of functional groups and modeling of their ionization behavior in the active layer of FT30 reverse osmosis membrane, Environ. Sci. Technol. 42 (2008) 5260–5266.

[41] H. Schwegmann, A.J. Feitz, F.H. Frimmel, Influence of the zeta potential on the sorption and toxicity of iron oxide nanoparticles on S. cerevisiae and E. coli, J. Colloid Interface Sci. 347 (2010) 43–48.

[42] N. Al-Janabi, P. Hill, L. Torrente-Murciano, A. Garforth, P. Gorgojo, F. Siperstein, X. Fan, Mapping the Cu-BTC metal–organic framework (HKUST-1) stability envelope in the presence of water vapour for CO2 adsorption from flue gases, Chem. Eng. J. 281 (2015) 669–677.

[43] M. Hu, B. Mi, Enabling graphene oxide nanosheets as water separation membranes, Environ. Sci. Technol. 47 (2013) 3715–3723.

[44] M. Aliabadi, M. Irani, J. Ismaeili, H. Piri, M.J. Parnian, Electrospun nanofiber membrane of PEO/Chitosan for the adsorption of nickel, cadmium, lead and copper ions from aqueous solution, Chem. Eng. J. 220 (2013) 237–243.

[45] M. Aliabadi, M. Irani, J. Ismaeili, S. Najafzadeh, Design and evaluation of chitosan/hydroxyapatite composite nanofiber membrane for the removal of heavy metal ions from aqueous solution, J. Taiwan. Inst. Chem. Eng. 45 (2014) 518–526.

[46] A. Razzaz, S. Ghorban, L. Hosayni, M. Irani, M. Aliabadi, Chitosan nanofibers functionalized by TiO2 nanoparticles for the removal of heavy metal ions, J. Taiwan. Inst. Chem. Eng. 58 (2016) 333–343.

[47] A. Ghaee, M. Shariaty-Niassar, J. Barzin, T. Matsuura, Effects of chitosan membrane morphology on copper ion adsorption, Chem. Eng. J. 165 (2010) 46–55.

[48] K.-H. Choo, H. Lee, S.-J. Choi, Iron and manganese removal and membrane fouling during UF in conjunction with prechlorination for drinking water treatment, J. Membr. Sci. 267 (2005) 18–26.

[49] B. Al-Rashdi, D. Johnson, N. Hilal, Removal of heavy metal ions by nanofiltration, Desalination 315 (2013) 2–17.

[50] N.A. Reiad, O.E.A. Salam, E.F. Abadir, F.A. Harraz, Adsorptive removal of iron and manganese ions from aqueous solutions with microporous chitosan/polyethylene glycol blend membrane, J. Environ. Sci. 24 (2012) 1425–1432.

[51] M. Shariful, T. Sepehr, M. Mehrali, B. Ang, M. Amalina, Adsorption capability of heavy metals by chitosan/poly (ethylene oxide)/activated carbon electrospun nanofibrous membrane, J. Appl. Polym. Sci. 135 (2018).

[52] B. Lam, S. Déon, N. Morin-Crini, G. Crini, P. Fievet, Polymer-enhanced ultrafiltration for heavy metal removal: influence of chitosan and carboxymethyl cellulose on filtration performances, J. Clean. Prod. 171 (2018) 927–933.

[53] E. Bagheripour, A. Moghadassi, S. Hosseini, B. Van der Bruggen, F. Parvizian, Novel composite graphene oxide/chitosan nanoplates incorporated into PES based nanofiltration membrane: chromium removal and antifouling enhancement, J. Ind. Eng. Chem. 62 (2018) 311–320.

[54] U. Habiba, A.M. Afifi, A. Salleh, B.C. Ang, Chitosan/(polyvinyl alcohol)/zeolite electrospun composite nanofibrous membrane for adsorption of Cr6+, Fe3+ and Ni2+, J. Hazard Mater. 322 (2017) 182–194.

[55] S. Koushkbaghi, A. Zakialamdari, M. Pishnamazi, H.F. Ramandi, M. Aliabadi, M. Irani, Aminated-Fe3O4 nanoparticles filled chitosan/PVA/PES dual layers nanofibrous membrane for the removal of Cr (VI) and Pb (II) ions from aqueous solutions in adsorption and membrane processes, Chem. Eng. J. 337 (2018) 169–182.

[56] M. Abu-Saied, R. Wycisk, M.M. Abbassy, G.A. El-Naim, F. El-Demerdash, M. Youssef, H. Bassuony, P.N. Pintauro, Sulfated chitosan/PVA absorbent membrane for removal of copper and nickel ions from aqueous solutions—fabrication and sorption studies, Carbohydr. Polym. 165 (2017) 149–158.

[57] M. Mazaheri, O. Akhavan, A. Simchi, Flexible bactericidal graphene oxide–chitosan layers for stem cell proliferation, Appl. Surf. Sci. 301 (2014) 456–462.

[58] Alireza Zirehpour, Ahmad Rahimpour, Ahmad Arabi Shamsabadi, Mohammad Sharifian Gh, Masoud Soroush, Mitigation of thin-film composite membrane biofouling via immobilizing nano-sized biocidal reservoirs in the membrane active layer, Environ. Sci. Technol. 51 (2017) 5511–5522.